Impacts of aerosol-photolysis interaction and aerosol-radiation feedback on surface-layer ozone in North China during multi-pollutant air pollution episodes

Hao Yang[1], Lei Chen[1], Hong Liao[1], Jia Zhu[1], Wenjie Wang[2], Xin Li[2]

[1]Jiangsu Key Laboratory of Atmospheric Environment Monitoring and Pollution Control, Jiangsu Collaborative Innovation Center of Atmospheric Environment and Equipment Technology, School of Environmental Science and Engineering, Nanjing University of Information Science & Technology, Nanjing 210044, China

[2]State Joint Key Laboratory of Environmental Simulation and Pollution Control, College of Environmental Sciences and Engineering, Peking University, Beijing 100871, China

Correspondence: Lei Chen (chenlei@nuist.edu.cn) and Hong Liao (hongliao@nuist.edu.cn)

Abstract

We examined the impacts of aerosol-radiation interactions, including the effects of aerosol-photolysis interaction (API) and aerosol-radiation feedback (ARF), on surface-layer ozone (O_3) concentrations during four multi-pollutant air pollution episodes characterized by high O_3 and $PM_{2.5}$ levels during 28 July to 3 August 2014 (Episode1), 8-13 July 2015 (Episode2), 5-11 June 2016 (Episode3), and 28 June to 3 July 2017 (Episode4) in North China, by using the Weather Research and Forecasting with Chemistry (WRF-Chem) model embedded with an integrated process analysis scheme. Our results show that API and ARF reduced the daytime shortwave radiative fluxes at the surface by 92.4~102.9 W m^{-2} and increased daytime shortwave radiative fluxes in the atmosphere by 72.8~85.2 W m^{-2}, as the values were averaged over the complex air pollution areas (CAPAs) in each of the four episodes. As a result, the stabilized atmosphere decreased the daytime planetary boundary layer height and 10 m wind speed by 129.0~249.0 m and 0.05~0.15 m s^{-1}, respectively, in CAPAs in the four episodes. Aerosols were simulated to reduce the daytime near-surface photolysis rates of $J[NO_2]$ and $J[O^1D]$ by 1.8×10^{-3}~2.0×10^{-3} s^{-1} and 5.7×10^{-6}~6.4×10^{-6} s^{-1}, respectively, in CAPAs in the four episodes. All the four episodes show the same conclusion that the reduction in O_3 by API is larger than that by ARF. API (ARF) was simulated to change daytime surface-layer O_3 concentrations by -8.5 ppb (-2.9 ppb), -10.3 ppb (-1.0 ppb), -9.1 ppb (-0.9 ppb) and -11.4 ppb (+0.7 ppb) in CAPAs of the four episodes, respectively. Process analysis indicated that the weakened O_3 chemical production made the greatest contribution to API effect, while the reduced vertical mixing was the key process for ARF effect. Our conclusions suggest that future $PM_{2.5}$ reductions may lead to O_3 increases due to the weakened aerosol-radiation interactions, which should be considered in air quality planning.

1 Introduction

The characteristics of air pollution in China during recent years are changing from the single pollutant (e.g., $PM_{2.5}$, particulate matter with an aerodynamic equivalent diameter of 2.5 μm or less) to multiple pollutants (e.g., $PM_{2.5}$ and ozone (O_3)) (Zhao et al., 2018; Zhu et al., 2019), and the synchronous occurrence of high $PM_{2.5}$ and O_3 concentrations has been frequently observed, especially during the warm seasons (Dai et al., 2021; Qin et al., 2021). Qin et al. (2021) reported that the co-occurrence of $PM_{2.5}$ and O_3 pollution days (days with $PM_{2.5}$ concentration > 75 μg m^{-3} as well as maximum daily 8 h average ozone concentration > 80 ppb) exceeded 324 days in eastern China during 2015-2019. Understanding the complex air pollution is essential for making plans to improve air quality in China.

Aerosols can influence O_3 by changing meteorology through absorbing and scattering solar radiation (defined as aerosol-radiation feedback (ARF) in this work) (Albrecht et al., 1989; Haywood et al., 2000; Lohmann et al., 2005), which influences air quality by altering the chemical reactions, transport and deposition of the pollutant (Gao et al., 2018; Qu et al., 2021; Xing et al., 2017; Zhang et al., 2018). Many studies examined the feedback between aerosols and meteorology (Gao et al., 2015; Gao et al., 2016a; Qiu et al., 2017; Chen et al., 2019; Zhu et al., 2021). For example, Gao et al. (2015) used the WRF-Chem model to investigate the feedbacks between aerosols and meteorological variables over the North China Plain in January 2013, and pointed out that aerosols caused a decrease in surface temperature by 0.8-2.8 °C but an increase of 0.1-0.5 °C around 925 hPa. By using the same WRF-Chem model, Qiu et al. (2017) reported that the surface downward shortwave radiation and PBLH were reduced by 54.6 W m^{-2} and 111.4 m, respectively, due to aerosol direct radiative effect during 21-27 February 2014 in the North China Plain. Such aerosol-induced changes in meteorological fields are expected to influence O_3 concentrations during multi-pollutant episodes with high concentrations of air pollutants.

Aerosols can also influence O_3 by altering photolysis rates (defined as aerosol-photolysis interaction (API) in this work) (Dickerson et al., 1997; Liao et al., 1999; Li

73   et al., 2011; Lou et al., 2014). Dickerson et al. (1997) reported that the presence of

74   pure scattering aerosol increased ground level ozone in the eastern United States by

75   20 to 45 ppb, while the presence of strongly absorbing aerosol reduced ground level

76   ozone by up to 24 ppb. Wang et al. (2019) found that aerosols reduced the net ozone

77   production rate by 25% by reducing the photolysis frequencies during a

78   comprehensive field observation in Beijing in August 2012. Such aerosol-induced

79   changes in photolysis rates are expected to influence O_3 concentrations during multi-

80   pollutant episodes with high concentrations of air pollutants.

81   Few previous studies quantified the effects of ARF and API on O_3 concentrations.

82   Xing et al. (2017) applied a two-way online coupled WRF-CMAQ model and

83   reported that the combination of API and ARF reduced the surface daily maximum 1

84   h O_3 (MDA1 O_3) by up to 39 $\mu g \, m^{-3}$ over China during January 2013. Qu et al. (2021)

85   found, by using the UK Earth System Model (UKESM1), that ARF reduced the

86   annual average surface O_3 by 3.84 ppb (14.9%) in the North China Plain during 2014.

87   Gao et al. (2020) analyzed the impacts of API on O_3 by using the WRF-Chem model

88   and reported that API reduced surface O_3 by 10.6 ppb (19.0%), 8.6 ppb (19.4%), and

89   8.2 ppb (17.7%) in Beijing, Tianjin, and Shijiazhuang, respectively, during October

90   2018. However, these previous studies mostly examined either ARF or API and did

91   not examine their total and respective roles in O_3 pollution in China. Furthermore,

92   these previous studies lacked process understanding about the impacts of ARF and

93   API on O_3 pollution under co-occurrence of $PM_{2.5}$ and O_3 pollution events.

94   The present study aims to quantify the respective/combined impacts of ARF and

95   API on surface O_3 concentrations by using the WRF-Chem model, and to identify the

96   prominent physical and/or chemical processes responsible for ARF and API effects by

97   using an integrated process rate (IPR) analysis embedded in the WRF-Chem model.

98   We carry on simulations and analyses on four multi-pollutant air pollution episodes

99   (Episode1: 28 July to 3 August 2014; Episode2: 8-13 July 2015; Episode3: 5-11 June

100 2016; Episode4, 28 June to 3 July 2017) in North China with high O_3 and $PM_{2.5}$ levels

101 (the daily mean $PM_{2.5}$ and the maximum daily 8-h average O_3 concentration are larger

102 than 75 $\mu g \, m^{-3}$ and 80 ppb, respectively). These episodes are selected because (1)

103 these events with high concentrations of both $PM_{2.5}$ and O_3 are the major subjects of

104 air pollution control, (2) high concentrations of both $PM_{2.5}$ and O_3 allow one to obtain

105 the strongest signals of ARF and API, (3) the measurements of $J[NO_2]$ during 2014

106 and 2015 from Peking University site (Wang et al., 2019) can help to constrain the

107 simulated photolysis rates of NO_2, and (4) selected events cover different years of

108 2014 to 2017 during which the governmental Air Pollution Prevention and Control

109 Action Plan was implemented (the changes in emissions and observed $PM_{2.5}$ in the

110 studied region during 2014-2017 are shown in Fig. S1). We expect that the

111 conclusions obtained from multiple episodes represent the general understanding of

112 the impacts of ARF and API.

113 The model configuration, numerical experiments, observational data, and the

114 integrated process rate analysis are described in section 2. Section 3 shows the model

115 evaluation. Results and discussions are presented in section 4, and the conclusions are

116 summarized in section 5.

2 Methods

2.1 Model configuration

119 The version 3.7.1 of the online-coupled Weather Research and Forecasting with

120 Chemistry (WRF-Chem) model (Grell et al., 2005; Skamarock et al., 2008) is used in

121 this study to explore the impacts of aerosol-radiation interactions on surface-layer O_3

122 in North China. WRF-Chem can simulate gas phase species and aerosols coupled with

123 meteorological fields, and has been widely used to investigate air pollution over North

124 China (Gao et al., 2016a; Gao et al., 2020; Wu et al., 2020). As shown in Fig. 1, we

125 design two nested model domains with the number of grid points of 57 (west–east) $\times$

126 41 (south–north) and 37 (west–east) $\times$ 43 (south–north) at 27 and 9 km horizontal

127 resolutions, respectively. The parent domain centers at (39 °N, 117 °E). The model

128 contains 29 vertical levels from the surface to 50 hPa, with 14 levels below 2 km for

129 the fully description of the vertical structure of planetary boundary layer (PBL).

130 The Carbon Bond Mechanism Z (CBM-Z) is selected as the gas-phase chemical

131 mechanism (Zaveri and Peters, 1999), and the full 8-bin MOSAIC (Model for

Simulating Aerosol Interactions and Chemistry) aerosol module with aqueous chemistry is used to simulate aerosol evolution (Zaveri et al., 2008). The photolysis rates are calculated by the Fast-J scheme (Wild et al., 2000). Other major physical parameterizations used in this study are listed in Table 1.

The initial and boundary meteorological conditions are provided by the National Centers for Environmental Prediction (NCEP) Final Analysis data with a spatial resolution of $1° \times 1°$. In order to limit the model bias of simulated meteorological fields, the four-dimensional data assimilation (FDDA) is used with the nudging coefficient of 3.0×10^{-4} for wind, temperature and humidity (no analysis nudging is applied for the inner domain) (Lo et al., 2008; Otte, 2008). Chemical initial and boundary conditions are obtained from the Model for Ozone and Related chemical Tracers, version 4 (MOZART-4) forecasts (Emmons et al., 2010).

Anthropogenic emissions in these four episodes are taken from the Multi-resolution Emission Inventory for China (MEIC) (http://www.meicmodel.org/) (Li et al., 2017a). These emission inventories provide emissions of sulfur dioxide (SO_2), nitrogen oxides (NO_x), carbon monoxide (CO), non-methane volatile organic compounds (NMVOCs), carbon dioxide (CO_2), ammonia (NH_3), black carbon (BC), organic carbon (OC), PM_{10} (particulate matter with aerodynamic diameter is 10 μm and less) and $PM_{2.5}$. Emissions are aggregated from four sectors, including power generation, industry, residential, and transportation, with $0.25° \times 0.25°$ spatial resolution. Biogenic emissions are calculated online by the Model of Emissions of Gases and Aerosols from Nature (MEGAN) (Guenther et al., 2006).

2.2 Numerical experiments

To quantify the impacts of API and ARF on O_3, three experiments have been conducted: (1) BASE – the base simulation coupled with the interactions between aerosol and radiation, which includes both impacts of API and ARF; (2) NOAPI – the same as the BASE case, but the impact of API is turned off (aerosol optical properties are set to zero in the photolysis module), following Wu et al. (2020); (3) NOALL – both the impacts of API and ARF are turned off (removing the mass of aerosol species

when calculating aerosol optical properties in the optical module), following Qiu et al. (2017). The differences between BASE and NOAPI (i.e., BASE minus NOAPI) represent the impacts of API. The contributions from ARF can be obtained by comparing NOAPI and NOALL (i.e., NOAPI minus NOALL). The combined effects of API and ARF on O_3 concentrations can be quantitatively evaluated by the differences between BASE and NOALL (i.e., BASE minus NOALL).

All the experiments in Episode1, Episode2, Episode3 and Episode4 are conducted from 26 July to 3 August 2014, 6-13 July 2015, 3-11 June 2016, and 26 June to 3 July 2017, respectively, with the first 40 hours as the model spin-up in each case. Simulation results from the BASE cases of the four episodes are used to evaluate the model performance.

2.3 Observational data

Simulation results are compared with meteorological and chemical measurements. The surface-layer meteorological data (2 m temperature (T_2), 2 m relative humidity (RH_2), and 10 m wind speed (WS_{10})) with the temporal resolution of 3 h at ten stations (Table S1) are obtained from NOAA's National Climatic Data Center (https://gis.ncdc.noaa.gov/maps/ncei/cdo/hourly). The radiosonde data of temperature at 08:00 and 20:00 LST in Beijing (39.93 °N, 116.28 °E) are provided by the University of Wyoming (http://weather.uwyo.edu/). Observed hourly concentrations of $PM_{2.5}$ and O_3 at thirty-two sites (Table S2) in North China are collected from the China National Environmental Monitoring Center (CNEMC). The photolysis rate of nitrogen dioxide ($J[NO_2]$) measured at the Peking University site (39.99 °N, 116.31 °E) is also used to evaluate the model performance. More details about the measurement technique of $J[NO_2]$ can be found in Wang et al. (2019). The aerosol optical depth (AOD) at Beijing site (39.98°N, 116.38°E) is provided by AERONET (level 2.0, http://aeronet.gsfc.nasa.gov/). The AOD at 675 nm and 440 nm are used to derive the AOD at 550 nm to compare with the simulated ones.

2.4 Integrated process rate analysis

Integrated process rate (IPR) analysis has been widely used to quantify the

190   contributions of different processes to O_3 variations (Goncalves et al., 2009; Gao et al.,

191   2016b; Tang et al., 2017; Gao et al., 2018). In this study, four physical/chemical

192   processes are considered, including vertical mixing (VMIX), net chemical production

193   (CHEM), horizontal advection (ADVH), and vertical advection (ADVZ). VMIX is

194   initiated by turbulent process and closely related to PBL development, which

195   influences O_3 vertical gradients. CHEM represents the net O_3 chemical production

196   (chemical production minus chemical consumption). ADVH and ADVZ represent

197   transport by winds (Gao et al., 2016b). In this study, we define ADV as the sum of

198   ADVH and ADVZ.

3 Model evaluation

200   Reasonable representation of observed meteorological and chemical variables by

201   the WRF-Chem model can provide foundation for evaluating the impacts of aerosols

202   on surface-layer ozone concentrations. The model results presented in this section are

203   taken from the BASE cases in the four episodes. The concentrations of air pollutants

204   are averaged over the thirty-two observation sites in Beijing, Tianjin and Baoding. To

205   ensure the data quality, the mean value for each time is calculated only when

206   concentrations are available at more than sixteen sites, as done in Li et al. (2019a).

3.1 Chemical simulations

208   Figure 2 shows the temporal variations of observed and simulated $PM_{2.5}$ and O_3

209   concentrations over North China for the four episodes. As shown in Fig. 2, the

210   temporal variations of observed $PM_{2.5}$ can be well performed by the model with index

211   of agreement (IOA) of 0.68, 0.68, 0.67 and 0.44 and normalized mean bias (NMB) of

212   -19.2%, 4.1%, 30.4% and 13.9% during Episode1, Episode2, Episode3 and Episode4,

213   respectively. The model also tracks well the diurnal variation of O_3 over the North

214   China, with IOA of 0.89, 0.94, 0.92 and 0.87 and NMB of -12.0%, -0.4%, 1.6% and -

215   13.8% for Episode1, Episode2, Episode3 and Episode4, respectively.

216   Figure S2 shows the correlation between observed and simulated AOD at 550

217   nm in Beijing. In the WRF-Chem model, the AOD at 550 nm are calculated by using

218   the values at 400 and 600 nm according to the Angstrom exponent. Analyzing Fig. S2,

219 the model can reproduce the observed AOD with R of 0.7 and NMB of 7.9%.

3.2 Meteorological simulations

221 Figure 3 shows the time series of observed and simulated T_2, RH_2, WS_{10} and $J[NO_2]$ during the four episodes. The observed T_2, RH_2, WS_{10} are averaged over the ten meteorological observation stations, and the $J[NO_2]$ are measured at Peking University. Most of the monitored $J[NO_2]$ in Episode3 and Episode4 are unavailable, so the comparison of $J[NO_2]$ in Episode3 and Episode4 is not shown. Generally, the model can depict the temporal variations of T_2 fairly well with IOA of 0.94~0.98 and the mean bias (MB) of -1.9~-0.6 °C. For RH_2, the IOA and MB are 0.90~0.98 and -6.5%~1.9%, respectively. Although WRF-Chem model overestimates WS_{10} with the MB of 0.6~1.0 m s^{-1}, the IOA for WS_{10} is 0.70~0.83 and the root-mean-square error (RMSE) is 0.9~1.5 m s^{-1}, which is smaller than the threshold of model performance criteria (2 m s^{-1}) proposed by Emery et al. (2001). The positive bias in wind speed can also be reproduced in other studies (Zhang et al., 2010; Gao et al., 2015; Liao et al., 2015; Qiu et al., 2017). The predicted $J[NO_2]$ agrees well with the observations with IOA of 0.98~0.99 and NMB of 6.8%~6.9%. We also conduct comparisons of observed and simulated temperature profiles at 08:00 and 20:00 LST in Beijing during the four episodes (Fig. S3). The vertical profiles of observed temperature can be well captured by the model in these four complex air pollution episodes. Generally, the WRF-Chem model can reasonably reproduce the temporal variations of observed meteorological parameters.

4 Results

241 We examine the impacts of aerosol-radiation interactions on O_3 concentrations with a special focus on the complex air pollution areas (CAPAs, Fig. S4) in the four episodes, where the daily mean simulated $PM_{2.5}$ and MDA8 (maximum daily 8-h average) O_3 concentrations are larger than 75 µg m^{-3} and 80 ppb, respectively, based on the National Ambient Air Quality Standards (http://www.mee.gov.cn).

4.1 Impacts of aerosol-radiation interactions on meteorology

9

247   Figure 4 shows the impacts of aerosol-radiation interactions on shortwave

248   radiation at the surface (BOT_SW), shortwave radiation in the atmosphere

249   (ATM_SW), PBLH, and WS_{10} during the daytime (08:00-17:00 LST) from Episode1

250   to Episode4. Analyzing the results of the interactions between aerosol and radiation

251   (the combined impacts of API and ARF), BOT_SW is decreased over the entire

252   simulated domain in the four episodes with the decreases of 93.2 W m^{-2} (20.5%),

253   100.3 W m^{-2} (19.5%), 92.4 W m^{-2} (19.2%) and 102.9 W m^{-2} (20.7%) over CAPAs,

254   respectively. Contrary to the changes in BOT_SW, ATM_SW is increased

255   significantly in the four episodes with the increases of 72.8 W m^{-2} (25.3%), 85.2 W m^{-2}

256   ^{2} (29.0%), 73.7 W m^{-2} (26.4%) and 76.9 W m^{-2} (25.8%) over CAPAs, respectively.

257   The decreased BOT_SW perturbs the near-surface energy flux, which weakens

258   convection and suppresses the development of PBL (Li et al., 2017b). The mean

259   PBLHs over CAPAs are decreased by 129.0 m (13.0%), 249.0 m (20.9%), 224.6 m

260   (19.0%) and 227.0 m (20.9%), respectively. WS_{10} exhibits overall reductions over

261   CAPAs and is calculated to decrease by 0.12 m s^{-1} (3.6%), 0.05 m s^{-1} (1.6%),0.12 m s^{-1}

262   ^{1} (3.0%) and 0.15 m s^{-1} (4.3%), for the four episodes, respectively. We also examine

263   the changed meteorological variables caused by API and ARF respectively. As shown

264   in Fig. S5 and S6, API has little impact on meteorological variables; which means the

265   major contributor to the meteorology variability is ARF.

266   **4.2 Impacts of aerosol-radiation interactions on photolysis**

267   Figure 5 shows the spatial distributions of mean daytime surface-layer $PM_{2.5}$

268   concentrations simulated by BASE cases and the changes in $J[NO_2]$ and $J[O^1D]$ due

269   to aerosol-radiation interactions from Episode1 to Episode4. When the combined

270   impacts (API and ARF) are considered, $J[NO_2]$ and $J[O^1D]$ are decreased over the

271   entire domain in the four episodes, and the spatial patterns of changed $J[NO_2]$ and

272    $J[O^1D]$ are similar to that of simulated $PM_{2.5}$. Analyzing the four simulated episodes,

273   the surface $J[NO_2]$ averaged over CAPAs are decreased by 1.8 × 10^{-3} s^{-1} (40.5%), 2.0

274   × 10^{-3} s^{-1} (36.8%), 1.8 × 10^{-3} s^{-1} (36.0%), and 2.0 × 10^{-3} s^{-1} (38.0%), respectively. The

275   decreased surface $J[O^1D]$ over CAPAs are 6.1 × 10^{-6} s^{-1} (48.8%), 6.3 × 10^{-6} s^{-1}

276 (41.4%), 5.7×10^{-6} s^{-1} (44.6%), and 6.4×10^{-6} s^{-1} (46.9%), respectively. Figure S7

277 exhibits the impacts of API and ARF on surface J[NO$_2$] and J[O^{1}D]. Conclusions can

278 be summarized that J[NO$_2$] and J[O^{1}D] are significantly modified by API and little

279 affected by ARF.

4.3 Impacts of aerosol-radiation interactions on O$_3$

281   Figure 6 shows the changes in surface-layer O$_3$ due to API, ARF, and the

282 combined effects (denoted as ALL) from Episode1 to Episode4. As shown in Fig.

283 6(a1-a4), API alone leads to overall surface O$_3$ decreases over the entire domain with

284 average reductions of 8.5 ppb (10.2%), 10.3 ppb (11.8%), 9.1 ppb (11.2%), and 11.4

285 ppb (12.2%) over CAPAs in the four episodes, respectively. The changes can be

286 explained by the substantially diminished UV radiation due to aerosol loading, which

287 significantly weakens the efficiency of photochemical reactions and restrains O$_3$

288 formation. However, the decreased surface O$_3$ concentrations due to ARF are only 2.9

289 ppb (3.2%, Fig. 6(b1)), 1.0 ppb (1.1%, Fig. 6(b2)) and 0.9 ppb (1.0%, Fig. 6(b3)) for

290 the Episode1 to Episode3 but ARF increased surface O$_3$ concentrations by 0.7 ppb

291 (0.5%, Fig.6(b4)) during Episode4, which was caused by the enhancement of

292 chemical production (Fig. S10 and Section 4.4). All the episodes show same

293 conclusion that the reduction in O$_3$ by API is larger than that by ARF. Fig. 6(c1-c4)

294 presents the combined effects of API and ARF. Generally, aerosol-radiation

295 interactions decrease the surface O$_3$ concentrations by 11.4 ppb (13.7%), 11.3 ppb

296 (13.0%), 10.0 ppb (12.3%) and 10.7 ppb (11.6%) averaged over CAPAs in the four

297 episodes, respectively.

4.4 Influencing mechanism of aerosol-radiation interactions on O$_3$

299   Figure 7a shows mean results of the four episodes (Episode1, Episode2,

300 Episode3 and Episode4) in diurnal variations of simulated daytime surface-layer O$_3$

301 concentrations from BASE, NOAPI and NOALL cases averaged over CAPAs. All the

302 experiments (BASE, NOAPI and NOALL) present O$_3$ increases from 08:00 LST. It is

303 shown that the simulated O$_3$ concentrations in BASE case increase more slowly than

304 that in NOAPI and NOALL cases. To explain the underlying mechanisms of API and

305 ARF impacts on O_3, we quantify the variations in contributions of different processes

306 (ADV, CHEM, and VMIX) to O_3 by using the IPR analysis.

307   Figure 7b shows hourly surface O_3 changes induced by each physical/chemical

308 process (i.e., ADV, CHEM, and VMIX) in BASE case averaged from Episode1 to

309 Episode4. The significant positive contribution to the hourly variation in O_3 is

310 contributed by VMIX, and the contribution reaches the maximum at about 09:00 LST.

311 Since VMIX increases the surface O_3 concentrations by transporting O_3 from aloft

312 (where O_3 concentrations are high) to the surface layer (Tang et al., 2017; Xing et al.,

313 2017; Gao et al., 2018). The CHEM process makes negative contributions at around

314 09:00 and 16:00 LST, which means that the chemical consumption of O_3 is stronger

315 than the chemical production. At noon, the net chemical contribution turns to be

316 positive due to stronger solar UV radiation. The contribution from all the processes

317 (NET, the sum of VMIX, CHEM, and ADV) to O_3 variation is peaked at the noon and

318 then becomes weakened. After sunset (17:00 LST), the NET contribution turns to be

319 negative over CAPAs, leading to O_3 decrease.

320   Figure 7c shows the changes in hourly process contributions caused by API

321 averaged from Episode1 to Episode4. The chemical production of O_3 is suppressed

322 significantly due to aerosol impacts on photolysis rates. The weakened O_3 chemical

323 production decreases the contribution from CHEM, and results in a negative value of

324 CHEM_DIF (-3.44 ppb h^{-1}). In contrast to CHEM_DIF, the contribution from

325 changed VMIX (VMIX_DIF) to O_3 concentration due to API is always positive, and

326 the mean value is +3.26 ppb h^{-1}. The positive change in VMIX due to API may be

327 associated with the different vertical gradient of O_3 between BASE and NOAPI cases

328 (Gao et al., 2020), as shown in Fig. 8a. The impact of API on ADV process is

329 relatively small (-0.26 ppb h^{-1}). NET_DIF, namely the sum of VMIX_DIF,

330 CHEM_DIF and ADV_DIF, indicates the differences in hourly O_3 changes caused by

331 API. As shown in Fig. 7c, NET_DIF is almost negative during the daytime over

332 CAPAs with the mean value of -0.44 ppb h^{-1}. This is because the decreases in CHEM

333 and ADV are larger than the increases in VMIX caused by API; the O_3 decrease is

334 mainly attributed to the significantly decreased contribution from CHEM. The

335 maximum difference in O_3 between BASE and NOAPI appears at 11:00 LST with a

336 value of -12.5 ppb (Fig. 7a).

337   Figure 7d shows the impacts of ARF on each physical/chemical process

338 contribution to the hourly O_3 variation averaged from Episode1 to Episode4. At 08:00

339 LST, the change in VMIX due to ARF is large with a value of -3.5 ppb h^{-1}, resulting in

340 a net negative variation with all processes considered. The decrease in O_3 reaches the

341 maximum with the value of 5.0 ppb at around 08:00 LST over CAPAs (Fig. 7a).

342 During 09:00 to 16:00 LST, the positive VMIX_DIF (mean value of +0.10 ppb h^{-1}) or

343 the positive CHEM_DIF (mean value of +0.75 ppb h^{-1}) is the major process to

344 positive NET_DIF. The positive VMIX_DIF is related to the evolution in boundary

345 layer during the daytime. The VOCs/NO_x ratio is calculated to classify sensitivity

346 regimes and to indicate the possible O_3 responses to changes in VOCs and/or NO_x

347 concentrations. O_3 production is VOC-limited if the ratio is less than 4, and is NO_x-

348 limited if the ratio is larger than 15 (Edson et al., 2017; Li et al., 2017c). The ratio of

349 VOCs/NO_x ranging around 4-15 indicates a transitional regime, where ozone is nearly

350 equally sensitive to both species (Sillman, 1999). As shown in Fig. S8, (a-f), O_3 is

351 mainly formed under the VOC-limited and the transition regimes in CAPAs. As

352 shown in Figs. S8(g-i) and S8(j-l), both the surface concentrations of VOCs and NO_x

353 are increased when the impacts of ARF are considered. Thus, the contribution of

354 CHEM in NOAPI is larger than that in NOALL.

355   When both impacts of API and ARF are considered, the variation pattern of the

356 difference in hourly process contribution shown in Fig. 7e is similar to that in Fig. 7c,

357 which indicates that API is the dominant factor to surface-layer O_3 reduction.

358   Figure 8 presents the vertical profiles of simulated daytime O_3 concentrations in

359 three cases (BASE, NOAPI, and NOALL), and the differences in contributions from

360 each physical/chemical process to hourly O_3 variations caused by API, ARF and the

361 combined effects averaged over CAPAs from Episode1 to Episode4. As shown in Fig.

362 8a, the O_3 concentration is lower in BASE than that in other two scenarios (NOAPI

363 and NOALL), especially at the lower 12 levels (below 801.8 m), owing to the impacts

364 of aerosols (API and/or ARF).

365   The changes in each process contribution caused by API are presented in Fig. 8b.

366   The contribution from CHEM_DIF is -2.1 ppb h^{-1} for the first seven layers (from 25.6

367   to 318.5 m). Conversely, the contribution from VMIX_DIF shows a positive value

368   under the 318.5 m (between the first layer to the seventh layer) with the mean value of

369   +1.8 ppb h^{-1}. The positive variation in VMIX due to API may be associated with the

370   different vertical gradient of O$_3$ between BASE and NOAPI again. The contributions

371   of changed advections (ADVH_DIF and ADVZ_DIF) are relatively small, with mean

372   values of +0.03 and -0.18 ppb h^{-1} below the first seven layers, which may result from

373   small impact of API on wind filed (Fig. S6(a4-d4)). The net difference is a negative

374   value (-0.45 ppb h^{-1}); API leads to O$_3$ reduction not only nearly surface but also aloft.

375   Figure 8c shows the differences in O$_3$ budget due to ARF. When the ARF is

376   considered, the vertical turbulence is weakened and the development of PBL is

377   inhibited, which makes VMIX_DIF negative at the lower seven layers (below the

378   318.5 m) with a mean value of -0.69 ppb h^{-1}, but the variation in CHEM caused by

379   ARF is positive with a mean value of +0.86 ppb h^{-1}. The enhanced O$_3$ precursors due

380   to ARF can promote the chemical production of O$_3$ (Tie et al., 2009; Gao et al., 2018).

381   The changes of ADVZ and ADVH (ADVZ_DIF and ADVH_DIF) caused by ARF are

382   associated with the variations in wind filed. When ARF is considered, the horizontal

383   wind speed is decreased (Fig. S9(a)), which makes ADVH_DIF positive at the lower

384   twelve layers with a mean value of +0.30 ppb h^{-1}. However, ADVZ_DIF is negative at

385   these layers with a mean value of -0.26 ppb h^{-1} because aerosol radiative effects

386   decrease the transport of O$_3$ from the upper to lower layers (Fig. S9(b)).

387   In Fig. 8d, the pattern and magnitude of the differences in process contributions

388   between BASE and NOALL are similar to those caused by API, indicating the

389   dominate contributor of API on O$_3$ changes. The impacts of API on O$_3$ both near the

390   surface and aloft are greater than those of ARF.

391   Figure S10 and S11 detailed show the influencing mechanism of aerosol-

392   radiation interactions on O$_3$ in each episode. Similar variation characteristics can be

393   found among the four episodes as the mean situation discussed above, with the larger

394   impacts of API on O$_3$ both near the surface and aloft than those of ARF, indicating the

395   role of API is much larger than that of ARF during all the simulated episodes.

396   **4.5 Discussions**

397   We presented above the results from our simulations of multi-pollutant air

398   pollution episodes. In order to make the conclusion be more general, we carried out

399   simulations for three additional air pollution conditions, i.e., (1) $PM_{2.5}$ pollution alone

400   (High_PM, with daily mean $PM_{2.5}$ concentration larger than 75 µg m^{-3}), (2) O_3

401   pollution alone (High_O$_3$, with the maximum daily 8-h average O_3 concentration

402   larger than 80 ppb), and (3) neither $PM_{2.5}$ nor O_3 exceeded air quality standard

403   (Low_POL, with daily mean $PM_{2.5}$ and the maximum daily 8-h average O_3

404   concentrations smaller than 75 µg m^{-3} and 80 ppb, respectively). For each condition of

405   air pollution, we examined two episodes.

406   Figures S12 and S13 show the temporal variations of observed and simulated

407    $PM_{2.5}$ and O_3 concentrations during 7-12 October 2014 (High_PM_Episode1), 7-11

408   April 2014 (High_PM_Episode2), 15-21 June 2017 (High_O$_3$_Episode1), 12-17 July

409   2017 (High_O$_3$_Episode2), 13-18 June 2016 (Low_POL_Episode1), and 13-17 July

410   2016 (Low_POL_Episode2). The temporal variations of observed $PM_{2.5}$ can be well

411   captured by the model with IOAs of 0.63, 0.82, 0.56, 0.42, 0.76 and 0.54, and NMBs

412   of 7.4%, 20.3%, -21.7%, -25.9%, 14.7% and -29.3% during High_PM_Episode1,

413   High_PM_Episode2, High_O$_3$_Episode1, High_O$_3$_Episode2, Low_POL_Episode1,

414   and Low_POL_Episode2, respectively. The model also simulates well the diurnal

415   variation of O_3 over the North China, with IOAs of 0.87, 0.80, 0.87, 0.90, 0.84 and

416   0.86, and NMBs of -9.4%, -29.5%, -15.2%, -9.4%, 11.6% and 18.0% in these six

417   episodes, respectively.

418   Figure 9 shows changes in daytime surface-layer O_3 due to API, ARF, and the

419   combined effects (denoted as ALL) of High_PM_Episode1, High_PM_Episode2,

420   High_O$_3$_Episode1,   High_O$_3$_Episode2,   Low_POL_Episode1,   and

421   Low_POL_Episode2. As summarized in Table 2, all the simulations confirm the same

422   conclusion that the reduction in O_3 by API is larger than that by ARF. Averaged over

423   the entire domain, the percentage reductions in O_3 by API and ARF are, respectively,

424 29.3% and 6.2% in High_PM_Episode1, 16.9% and 4.7% in High_PM_Episode2, 5.3%

425 and 0.1% in High_O$_3$_Episode1, 4.5% and 0.1% in High_O$_3$_Episode2, 6.8% and 1.0%

426 in Low_POL_Episode1, and 2.9% and 0.7% in Low_POL_Episode2. It's worth

427 noting that the percentage reductions in O$_3$ from both API and ARF in High_PM

428 episodes are 1.6~3.2 times the impacts in the complex episodes, while the impacts in

429 cases of Low_POL and High_O$_3$ are 0.3~0.7 times the impacts of complex episodes."

5 Conclusions

431 In this study, the fully coupled regional chemistry transport model WRF-Chem is

432 applied to investigate the impacts of aerosol-radiation interactions, including the

433 impacts of aerosol-photolysis interaction (API) and the impacts of aerosol-radiation

434 feedback (ARF), on O$_3$ during summertime complex air pollution episodes during 28

435 July to 3 August 2014 (Episode1), 8-13 July 2015 (Episode2), 5-11 June 2016

436 (Episode3) and 28 June to 3 July 2017 (Episode4). Three sensitivity experiments are

437 designed to quantify the respective and combined impacts from API and ARF.

438 Generally, the spatiotemporal distributions of observed pollutant concentrations and

439 meteorological parameters can be captured fairly well by the model with index of

440 agreement of 0.44~0.94 for pollutant concentrations and 0.70~0.99 for meteorological

441 parameters.

442 Sensitivity experiments show that aerosol-radiation interactions decrease

443 BOT_SW, WS$_{10}$, PBLH, J[NO$_2$], and J[O^{1}D] by 92.4~102.9 W m^{-2}, 0.05~0.15 m s^{-1},

444 129.0~249.0 m, 1.8×10^{-3}~2.0×10^{-3} s^{-1}, and 5.7×10^{-6}~6.4×10^{-6} s^{-1} over CAPAs,

445 and increase ATM_SW by 72.8~85.2 W m^{-2}, respectively. The changed

446 meteorological variables and weakened photochemistry reaction further reduce

447 surface-layer O$_3$ concentrations by 10.0~11.4 ppb, with relative changes of

448 74.6%~106.5% by API and of -6.5%~25.4% by ARF.

449 We further examine the influencing mechanism of aerosol-radiation interactions

450 on O$_3$ by using integrated process rate analysis. API can directly affect O$_3$ by reducing

451 the photochemistry reactions within the lower several hundred meters and therefore

452 amplify the O$_3$ vertical gradient, which promotes the vertical mixing of O$_3$. The

16

453   reduced photochemistry reactions of O_3 weaken the chemical contribution and reduce

454   surface O_3 concentrations, even though the enhanced vertical mixing can partly

455   counteract the reduction. ARF affects O_3 concentrations indirectly through the

456   changed meteorological variables, e.g., the decreased PBLH. The suppressed PBL can

457   weaken the vertical mixing of O_3 by turbulence. Generally, the impacts of API on O_3

458   both near the surface and aloft are greater than those of ARF, indicating the dominant

459   role of API on O_3 reduction related with aerosol-radiation interactions.

460   This study provides a detailed understanding of aerosol impacts on O_3 through

461   aerosol-radiation interactions (including both API and ARF), with the general

462   conclusion summarized as follows: when the impacts of aerosol-radiation interactions

463   are considered, the changed meteorological variables and weakened photochemistry

464   reaction can change surface-layer O_3 concentrations during the warm season, and the

465   API is the dominant factor for O_3 reduction. The results can also imply that future

466     $PM_{2.5}$ reductions may lead to O_3 increases due to weakened aerosol-radiation

467   interactions. A recent study emphasized the need for controlling VOCs emissions to

468   mitigate O_3 pollution (Li et al., 2019b). Therefore, tighter controls of O_3 precursors

469   (especially VOCs emissions) are needed to counteract future O_3 increases caused by

470   weakened aerosol-radiation interactions.

471   There are some limitations in this work. (1) In the current CBMZ and MOSAIC

472   schemes, the formation of SOA (secondary organic aerosol) is not included (Gao et al.,

473   2015; Chen et al., 2019). The absence of SOA can underestimate the impacts of API

474   and ARF on O_3. Meanwhile, the lack of SOA may lead to weaker heterogeneous

475   reactions to result in higher O_3 concentrations (Li et al., 2019c). The net effect of the

476   two processes will be discussed and quantified in our future study. (2) The CNEMC

477   network was built in 2013. Before 2013, the national observations of $PM_{2.5}$ and O_3

478   concentrations were not available, which make it difficult to select the time and area

479   of complex air pollution events and to evaluate the model results. Based on

480   observation data, we were mainly focused on impacts of ARF and API on surface O_3

481   for complex air pollution episodes from 2014 to 2017. Additional simulations of

482   High_PM, High_O_3, and Low_POL support the conclusion obtained from the

483   complex air pollution episodes that the reduction in O_3 by API is larger than that by

484   ARF.

485

Data availability

The observed hourly surface concentrations of air pollutants are derived from the China National Environmental Monitoring Center (http://www.cnemc.cn). The observed surface meteorological data are obtained from NOAA's National Climatic Data Center (https://gis.ncdc.noaa.gov/maps/ncei/cdo/hourly). The radiosonde data are provided by the University of Wyoming (http://weather.uwyo.edu/). The photolysis rates of nitrogen dioxide in Beijing are provided by Xin Li (li_xin@pku.edu.cn). The aerosol optical depth in Beijing is obtained from the AERONET level 2.0 data collection (http://aeronet.gsfc.nasa.gov/). The simulation results can be accessed by contacting Lei Chen (chenlei@nuist.edu.cn) and Hong Liao (hongliao@nuist.edu.cn).

Author contributions

HY, LC, and HL conceived the study and designed the experiments. HY and LC performed the simulations and carried out the data analysis. JZ, WW, and XL provided useful comments on the paper. HY, LC, and HL prepared the paper with contributions from all co-authors.

Competing interests

The authors declare that they have no competing interests.

Acknowledgements

514   their support of this work.

Reference

Albrecht, B. A.: Aerosols, cloud microphysics, and fractional cloudiness, Science, 245, 1227–1230, 1989.

Chen, F. and Dudhia, J.: Coupling an Advanced Land Surface – Hydrology Model with the Penn State – NCAR MM5 Modeling System. Part I: Model Implementation and Sensitivity, Mon. Weather Rev., 129(4), 569–585, 2001.

Chen, L., Zhu, J., Liao, H., Gao, Y., Qiu, Y., Zhang, M., Liu, Z., Li, N., and Wang, Y.: Assessing the formation and evolution mechanisms of severe haze pollution in the Beijing–Tianjin–Hebei region using process analysis, Atmos. Chem. Phys., 19, 10845–10864, https://doi.org/10.5194/acp-19-10845-2019, 2019.

Dai, H., Zhu, J., Liao, H., Li, J., Liang, M., Yang, Y., and Yue, X.: Co-occurrence of ozone and $PM_{2.5}$ pollution in the Yangtze River Delta over 2013–2019: Spatiotemporal distribution and meteorological conditions, Atmos. Res., 249, 105363, 2021.

Dickerson, R. R., Kondragunta, S., Stenchikov, G., Civerolo, K. L., Doddridge, B. G., and Holben, B. N.: The impact of aerosols on solar ultraviolet radiation and photochemical smog, Science, 278, 827-830, 10.1126/science.278.5339.827, 1997.

Edson, C. T., Ivan, H.-P. and Alberto, M.: Use of combined observational- and model-derived photochemical indicators to assess the O_3-NOx-VOC System sensitivity in urban areas, Atmosphere., 8, 22. https://doi.org/10.3390/atmos8020022, 2017.

Emery, C., Tai, E., and Yarwood, G.: Enhanced meteorological modeling and performance evaluation for two Texas ozone episodes, in: Prepared for the Texas Natural Resource Conservation Commission, ENVIRON International Corporation, Novato, CA, USA, 2001.

Emmons, L. K., Walters, S., Hess, P. G., Lamarque, J.-F., Pfister, G. G., Fillmore, D., Granier, C., Guenther, A., Kinnison, D., Laepple, T., Orlando, J., Tie, X., Tyndall, G., Wiedinmyer, C., Baughcum, S. L., and Kloster, S.: Description and evaluation of the Model for Ozone and Related chemical Tracers, version 4 (MOZART-4),

Geosci. Model Dev., 3, 43–67, doi:10.5194/gmd- 3-43-2010, 2010.

Foken, T.: 50 years of the Monin-Obukhov similarity theory, Bound.-Layer Meteor., 119, 431–437, 2006.

Gao, J., Li, Y., Zhu, B., Hu, B., Wang, L., and Bao, F.: What have we missed when studying the impact of aerosols on surface ozone via changing photolysis rates?, Atmos. Chem. Phys., 20, 10831–10844, https://doi.org/10.5194/acp-20-10831-2020, 2020.

Gao, J. H., Zhu, B., Xiao, H., Kang, H. Q., Pan, C., Wang, D. D., and Wang, H. L.: Effects of black carbon and boundary layer interaction on surface ozone in Nanjing, China, Atmos. Chem. Phys., 18, 7081–7094, https://doi.org/10.5194/acp-18-7081-2018, 2018.

Gao, M., Carmichael, G. R., Wang, Y., Saide, P. E., Yu, M., Xin, J., Liu, Z., and Wang, Z.: Modeling study of the 2010 regional haze event in the North China Plain, Atmos. Chem. Phys., 16, 1673–1691, doi:10.5194/acp-16-1673-2016, 2016a.

Gao, J., Zhu, B., Xiao, H., Kang, H., Hou, X., and Shao, P.: A case study of surface ozone source apportionment during a high concentration episode, under frequent shifting wind conditions over the Yangtze River Delta, China, Sci. Total Environ., 544, 853, https://doi.org/10.1016/j.scitotenv.2015.12.039, 2016b.

Gao, Y., Zhang, M., Liu, Z., Wang, L., Wang, P., Xia, X., Tao, M., and Zhu, L.: Modeling the feedback between aerosol and meteorological variables in the atmospheric boundary layer during a severe fog–haze event over the North China Plain, Atmos. Chem. Phys., 15, 4279–4295, doi:10.5194/acp-15-4279-2015, 2015.

Goncalves, M., Jimenez-Guerrero, P., Baldasano, J.M.: Contribution of atmospheric processes affecting the dynamics of air pollution in South-Western Europe during a typical summertime photochemical episode, Atmos. Chem. Phys., 9, 849‒864, doi:10.5194/acp-9-849-2009, 2009.

Grell, G. A., Peckham, S. E., Schmitz, R., Mckeen, S. A., Frost, G., Skamarock, K., and Eder, B.: Fully coupled "online" chemistry within the WRF model, Atmos. Environ., 39, 6957–6975, 2005.

Guenther, A., Karl, T., Harley, P., Wiedinmyer, C., Palmer, P. I., and Geron, C.:

Estimates of global terrestrial isoprene emissions using MEGAN (Model of Emissions of Gases and Aerosols from Nature), Atmos. Chem. Phys., 6, 3181–3210, doi:10.5194/acp-6-3181-2006, 2006.

Haywood, J. and Boucher, O.: Estimates of the direct and indirect radiative forcing due to tropospheric aerosols: A review, Rev. Geophys., 38, 513–543, 2000.

Hong, S.-Y., Noh, Y., and Dudhia, J.: A New Vertical Diffusion Package with an Explicit Treatment of Entrainment Processes, Mon. Weather Rev., 134, 2318–2341, 2006.

Iacono, M. J., Delamere, J. S., Mlawer, E. J., Shephard, M. W., Clough, S. A., and Collins, W. D.: Radiative forcing by long-lived greenhouse gases: Calculations with the AER radiative transfer models, J. Geophys. Res., 113, D13103, doi:10.1029/2008JD009944, 2008.

Li, G., Bei, N., Tie, X., and Molina, L. T.: Aerosol effects on the photochemistry in Mexico City during MCMA-2006/MILAGRO campaign, Atmos Chem Phys, 11, 5169-5182, 10.5194/acp-11-5169-2011, 2011.

Li, J. D., Liao, H., Hu, J. L., Li, N.: Severe particulate pollution days in China during 2013-2018 and the associated typical weather patterns in Beijing-Tianjin-Hebei and the Yangtze River Delta regions, *Environmental Pollution*, 248, 74-81, 2019a.

Li, K., Jacob, D. J., Liao, H., Zhu, J., Shah, V., Shen, L., Bates, K. H., Zhang, Q., and Zhai, S.: A two-pollutant strategy for improving ozone and particulate air quality in China, Nat. Geosci., 12, 906–910, https://doi.org/10.1038/s41561-019-0464-x, 2019b.

Li, K., Jacob, D. J., Liao, H., Shen, L., Zhang, Q., and Bates, K. H.: Anthropogenic drivers of 2013–2017 trends in summer surface ozone in China, P. Natl. Acad. Sci. USA, 116, 422–427, https://doi.org/10.1073/pnas.1812168116, 2019c.

Li, M., Zhang, Q., Kurokawa, J.-I., Woo, J.-H., He, K., Lu, Z., Ohara, T., Song, Y., Streets, D. G., Carmichael, G. R., Cheng, Y., Hong, C., Huo, H., Jiang, X., Kang, S., Liu, F., Su, H., and Zheng, B.: MIX: a mosaic Asian anthropogenic emission inventory under the international collaboration framework of the MICS-Asia and HTAP, Atmos. Chem. Phys., 17, 935–963, https://doi.org/10.5194/acp-17-935-2017,

604   2017a.

605   Li, Z., Guo, J., Ding, A., Liao, H., Liu, J., Sun, Y., Wang, T., Xue, H., Zhang, H., and

606   Zhu, B.: Aerosol and boundary-layer interactions and impact on air quality, Nat. Sci.

607   Rev., 4, 810–833, https://doi.org/10.1093/nsr/nwx117, 2017b.

608   Li, K., Chen, L., Ying, F., White, S. J., Jang, C., Wu, X., Gao, X., Hong, S., Shen, J.,

609   Azzi, M. and Cen, K: Meteorological and chemical impacts on ozone formation: a

610   case study in Hangzhou, China, Atmos. Res., 196, https://doi.org/10.1016/

611   j.atmosres.2017.06.003, 2017c.

612   Liao, H., Yung, Y. L., and Seinfeld, J. H.: Effects of aerosols on tropospheric

613   photolysis rates in clear and cloudy atmospheres, J. Geophys. Res., 104, 23697–

614   23707, 1999.

615   Liao, L., Lou, S. J., Fu, Y., Chang, W. Y., and Liao, H.: Radiative forcing of aerosols

616   and its impact on surface air temperature on the synoptic scale in eastern China [in

617   Chinese], Chin. J. Atmos. Sci., 39, 68–82, doi: 10.3878/j.issn.1006-

618   9895.1402.13302, 2015.

619   Lin, Y.-L., Farley, R. D., and Orville, H. D.: Bulk parameterization of the snow field

620   in a cloud model, J. Clim. Appl. Meteorol., 22, 1065–1092, 1983.

621   Lo, J. C.-F., Yang, Z. L., and Pielke Sr, R. A.: Assessment of three dynamical climate

622   downscaling methods using the Weather Research and Forecasting (WRF) model, J.

623   Geophys. Res., 113, D09112, doi:10.1029/2007jd009216, 2008.

624   Lohmann, U., and Feichter, J.: Global indirect aerosol effects: A review. Atmospheric

625   Chemistry and Physics, 5, 715–737, https://doi.org/10.5194/acp-5-715-2005, 2005.

626   Lou, S., Liao, H., and Zhu, B.: Impacts of aerosols on surface-layer ozone

627   concentrations in China through heterogeneous reactions and changes in photolysis

628   rates, Atmos. Environ., 85, 123–138, 2014.

629   Otte, T. L.: The impact of nudging in the meteorological model for retrospective air

630   quality simulations. Part I: Evaluation against national observation networks. J.

631   Appl. Meteor. Climatol., 47, 1853–1867, 2008.

632   Qin, Y., Li, J., Gong, K., Wu, Z., Chen, M., Qin, M., Huang, L., and Hu, J.: Double

633   high pollution events in the Yangtze River Delta from 2015 to 2019: Characteristics,

trends, and meteorological situations, Sci. Total Environ., 792, 148349, 2021.

Qiu, Y., Liao, H., Zhang, R., and Hu, J.: Simulated impacts of direct radiative effects of scattering and absorbing aerosols on surface layer aerosol concentrations in China during a heavily polluted event in February 2014, J. Geophys. Res. Atmos., 122, 5955–5975, doi:10.1002/2016JD026309, 2017.

Qu, Y., Voulgarakis, A., Wang, T., Kasoar, M., Wells, C., Yuan, C., Varma, S., and Mansfield, L.: A study of the effect of aerosols on surface ozone through meteorology feedbacks over China, Atmos. Chem. Phys., 21, 5705–5718, https://doi.org/10.5194/acp-21-5705-2021, 2021.

Sillman, S.: The relation between ozone, NO_x and hydrocarbons in urban and polluted rural environments, Atmos. Environ., 33, 1821-1845, https://doi.org/10.1016/S1352-2310(98)00345-8, 1999.

Skamarock, W., Klemp, J. B., Dudhia, J., Gill, D. O., Barker, D. M., Duda, M., Huang, X. Y., Wang,W., and Powers, J. G.: A description of the advanced research WRF version 3, NCAR technical note NCAR/TN/u2013475, 2008.

Tang, G. Q., Zhu, X.W., Xin, J. Y., Hu, B., Song, T., Sun, Y., Zhang, J. Q., Wang, L. L., Cheng, M. T., Chao, N., Kong, L. B., Li, X., and Wang, Y. S.: Modelling study of boundary-layer ozone over northern China – Part I: Ozone budget in summer, Atmos. Res., 187, 128–137, 2017.

Tie, X., Geng, F., Li, P., Gao, W., and Zhao, C.: Measurement and modelling of ozone variability in Shanghai, China, Atmos. Environ., 43, 4289–4302, 2009.

Wang, W., Li, X., Shao, M., Hu, M., Zeng, L., Wu, Y., and Tan, T.: The impact of aerosols on photolysis frequencies and ozone production in Beijing during the 4-year period 2012–2015, Atmos. Chem. Phys., 19, 9413–9429, https://doi.org/10.5194/acp19-9413-2019, 2019.

Wild, O., Zhu, X., and Prather, M. J.: Fast-J: Accurate simulation of in- and below-cloud photolysis in tropospheric chemical models, J. Atmos. Chem., 37, 245–282, doi:10.1023/A:1006415919030, 2000.

Wu, J., Bei, N., Hu, B., Liu, S., Wang, Y., Shen, Z., Li, X., Liu, L., Wang, R., Liu, Z., Cao, J., Tie, X., Molina, L. T., Li, G.: Aerosol-photolysis interaction reduces

664   particulate matter during wintertime haze events, Proc. Natl. Acad. Sci. USA, 117,

665   9755–9761, 2020.

666 Xing, J., Wang, J. D., Mathur, R., Wang, S. X., Sarwar, G., Pleim, J., Hogrefe, C.,

667   Zhang, Y. Q., Jiang, J. K., Wong, D. and Hao, J. M.: Impacts of aerosol direct

668   effects on tropospheric ozone through changes in atmospheric dynamics and

669   photolysis rates, Atmos. Chem. Phys., 17, 9869–9883, https://doi.org/10.5194/acp-

670   17-9869-2017, 2017.

671 Zaveri, R. A. and Peters, L. K.: A new lumped structure photochemical mechanism

672   for large-scale applications, J. Geophys. Res., 104, D23, 30387–30415,

673   https://doi.org/10.1029/1999JD900876, 1999.

674 Zaveri, R. A., Easter, R. C., Fast, J. D., and Peters, L. K.: Model for simulating

675   aerosol interactions and chemistry (MOSAIC), J. Geophys. Res., 113, D13204,

676   https://doi.org/10.1029/2007JD008782, 2008.

677 Zhang, X., Zhang, Q., Hong, C. P., Zheng, Y. X., Geng, G. N., Tong, D., Zhang, Y. X.,

678   and Zhang, X. Y.: Enhancement of $PM_{2.5}$ concentrations by aerosol-meteorology

679   interactions over China. Journal of Geophysical Research: Atmospheres,123, 1179–

680   1194, https://doi.org/10.1002/2017JD027524, 2018.

681 Zhang, Y., Wen, X.-Y., and Jang, C. J.: Simulating chemistry–aerosol–cloud–

682   radiation–climate feedbacks over the continental US using the online-coupled

683   Weather Research Forecasting Model with chemistry (WRF/Chem), Atmos.

684   Environ., 44, 3568–3582, doi:10.1016/j.atmosenv.2010.05.056, 2010.

685 Zhao, H.; Zheng, Y., and Li, C. Spatiotemporal distribution of $PM_{2.5}$ and O_3 and their

686   interaction during the summer and winter seasons in Beijing, China. Sustainability,

687   10, 4519, 2018.

688 Zhu, J., Chen, L., Liao, H., and Dang, R.: Correlations between $PM_{2.5}$ and Ozone over

689   China and Associated Underlying Reasons, Atmosphere, 352, 1–15,

690   https://doi.org/10.3390/atmos10070352, 2019.

691 Zhu, J., Chen, L., Liao, H., Yang, H., Yang, Y., and Yue, X.: Enhanced $PM_{2.5}$

692   Decreases and O_3 Increases in China During COVID-19 Lockdown by Aerosol-

693   Radiation Feedback, Geophys. Res. Lett., 48,

694   https://doi.org/10.1029/2020GL090260, 2021.

1   **Table 1.** Physical parameterization options used in the simulation.

Options	Schemes
Microphysics scheme	Lin (Purdue) scheme (Lin et al.,1983)
Cumulus scheme	Grell 3D ensemble scheme
Boundary layer scheme	Yonsei University PBL scheme (Hong et al., 2006)
Surface layer scheme	Monin-Obukhov surface scheme (Foken, 2006)
Land-surface scheme	Unified Noah land-surface model (Chen and Dudhia, 2001)
Longwave radiation scheme	RRTMG (Iacono et al., 2008)
Shortwave radiation scheme	RRTMG (Iacono et al., 2008)

2

1 **Table 2.** Detailed information of the analyzed episodes, including the impacts of API, ARF and ALL on O_3 concentrations under different air
2 pollution conditions. The numbers in bold indicate the concentrations exceeded the Class II limit of the National Ambient Air Quality Standards
3 of China. The numbers in parentheses indicate the percentage changes in O_3 concentration.

| Type	Episode	Time	PM$_{2.5}$ pollution ($\mu g\ m^{-3}$)	O$_3$ pollution (ppb)	API (ppb)	ARF (ppb)	ALL (ppb)
Complex air pollution	Episode1	2014.7.28-2014.8.3	**113.3**	**80.0**	-8.5 (-10.2%)	-2.9 (-3.2%)	-11.4 (-13.7%)
	Episode2	2015.7.8-2015.7.13	**79.3**	**89.6**	-10.3 (-11.8%)	-1.0 (-1.1%)	-11.3 (-13.0%)
	Episode3	2016.6.5-2016.6.11	**76.5**	**87.6**	-9.1 (-11.2%)	-0.9 (-1.0%)	-10.0 (-12.3%)
	Episode4	2017.6.28-2017.7.3	**75.4**	**113.8**	-11.4 (-12.2%)	0.7 (0.5%)	-10.7 (-11.6%)
High_PM	Episode1	2014.10.7-2014.10.12	**223.5**	46.9	-15.3 (-29.3%)	-3.9 (-6.2%)	-19.2 (-37.6%)
	Episode2	2014.4.7-2014.4.11	**111.7**	54.8	-7.3 (-16.9%)	-2.4 (-4.7%)	-9.7 (-22.6%)
High_O$_3$	Episode1	2017.6.15-2017.6.21	61.9	**103.6**	-4.5 (-5.3%)	-0.1 (-0.1%)	-4.6 (-5.5%)
	Episode2	2017.7.12-2017.7.17	45.6	**100.4**	-3.8 (-4.5%)	-0.1 (-0.1%)	-3.9 (-4.6%)
Low_POL	Episode1	2016.6.13-2016.6.18	36.5	62.4	-4.4 (-6.8%)	-0.6 (-1.0%)	-5.0 (-7.9%)
	Episode2	2016.7.13-2016.7.17	38.3	55.9	-1.9 (-2.9%)	-0.5 (-0.7%)	-2.4 (-3.7%)

4
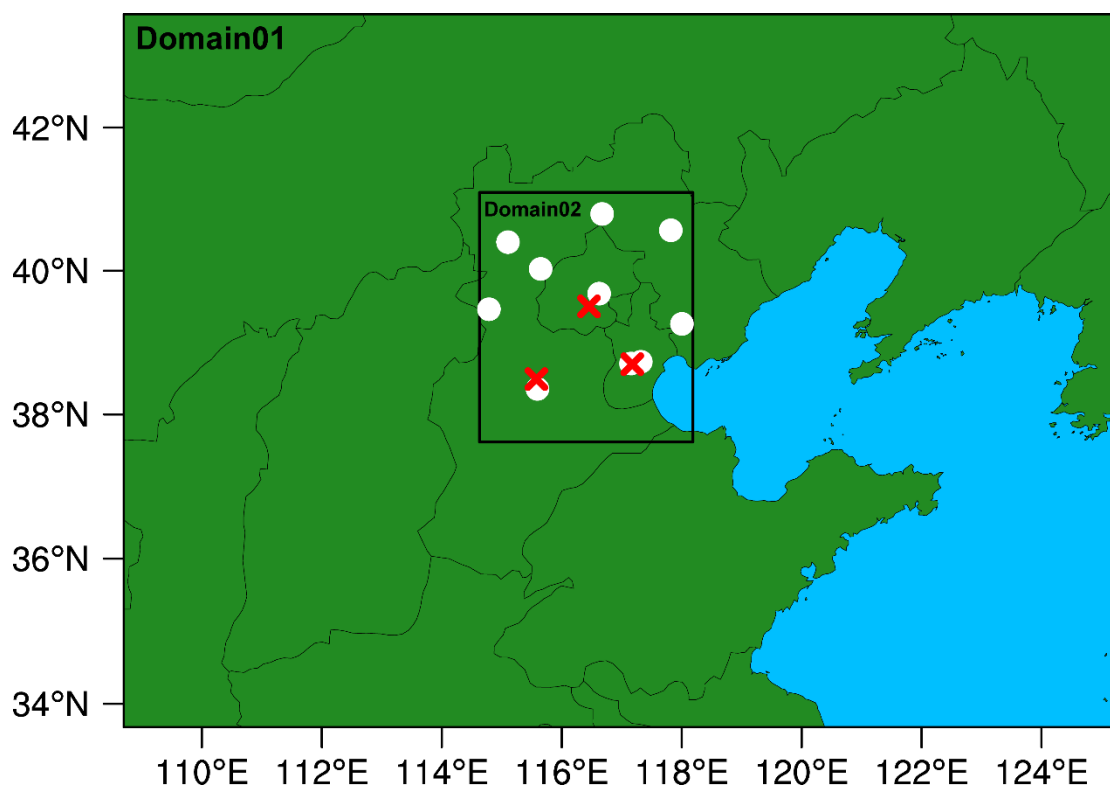
Figure 1. Map of the two WRF-Chem modeling domains with the locations of meteorological (white dots) and environmental (red crosses) observation sites used for model evaluation.
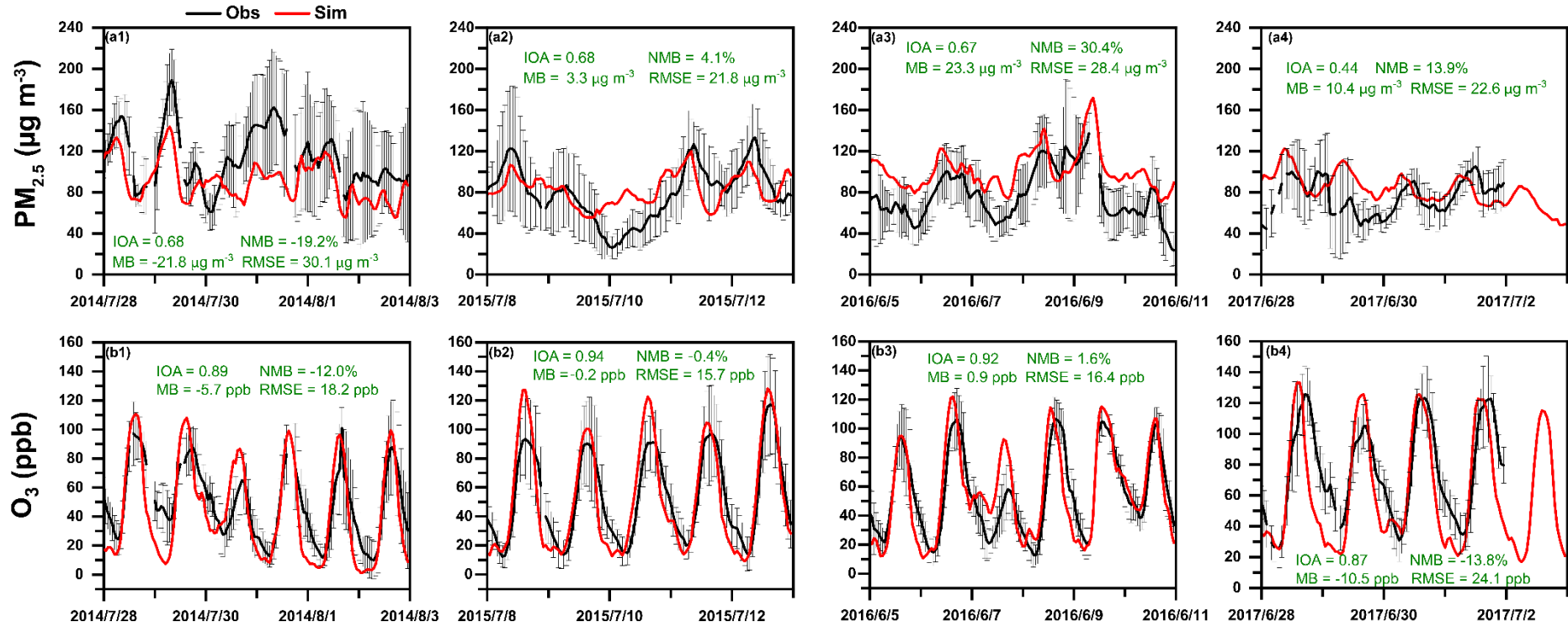
Figure 2. Time series of observed (black) and simulated (red) hourly surface (a) PM$_{2.5}$ and (b) O$_3$ concentrations averaged over the thirty-two observation sites in Beijing, Tianjin, and Baoding during 28 July to 3 August 2014 (Episode1, a1-b1), 8-13 July 2015 (Episode2, a2-b2), 5-11 June 2016 (Episode3, a3-b3) and 28 June to 3 July 2017 (Episode4, a4-b4). The error bars represent the standard deviations. The calculated index of agreement (IOA), mean bias (MB), normalized mean bias (NMB) and root-mean-square error (RMSE) are also shown.

1
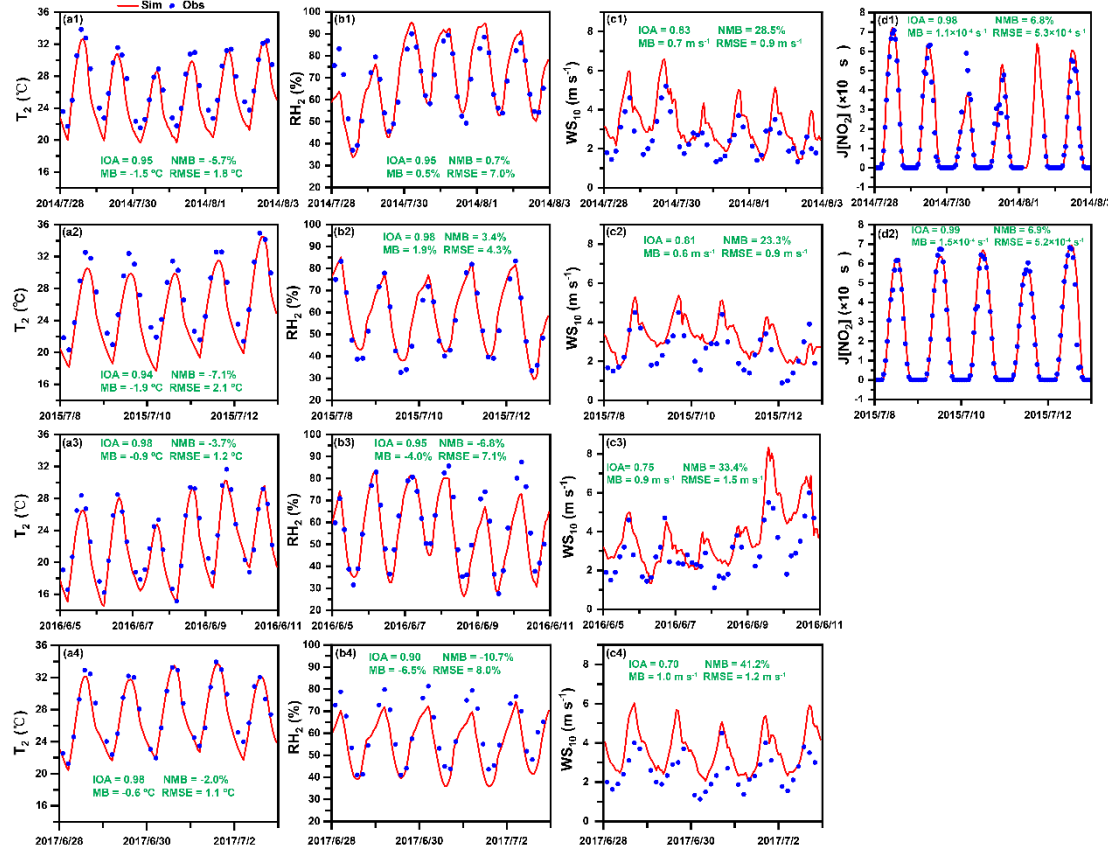
**Figure 3.** Time series of 3-hourly observed (blue dots) and hourly simulated (red lines) (a) 2-m temperature (T_2), (b) 2-m relative humidity (RH_2), (c) wind speed at 10 m (WS_{10}) averaged over ten meteorological observation stations, and (d) surface photolysis rate of NO_2 ($J[NO_2]$) during 28 July to 3 August 2014 (Episode1, a1-d1), 8-13 July 2015 (Episode2, a2-d2), 5-11 June 2016 (Episode3, a3-c3) and 28 June to 3 July 2017 (Episode4, a4-c4). The calculated index of agreement (IOA), mean bias (MB), normalized mean bias (NMB) and root-mean-square error (RMSE) are also shown.
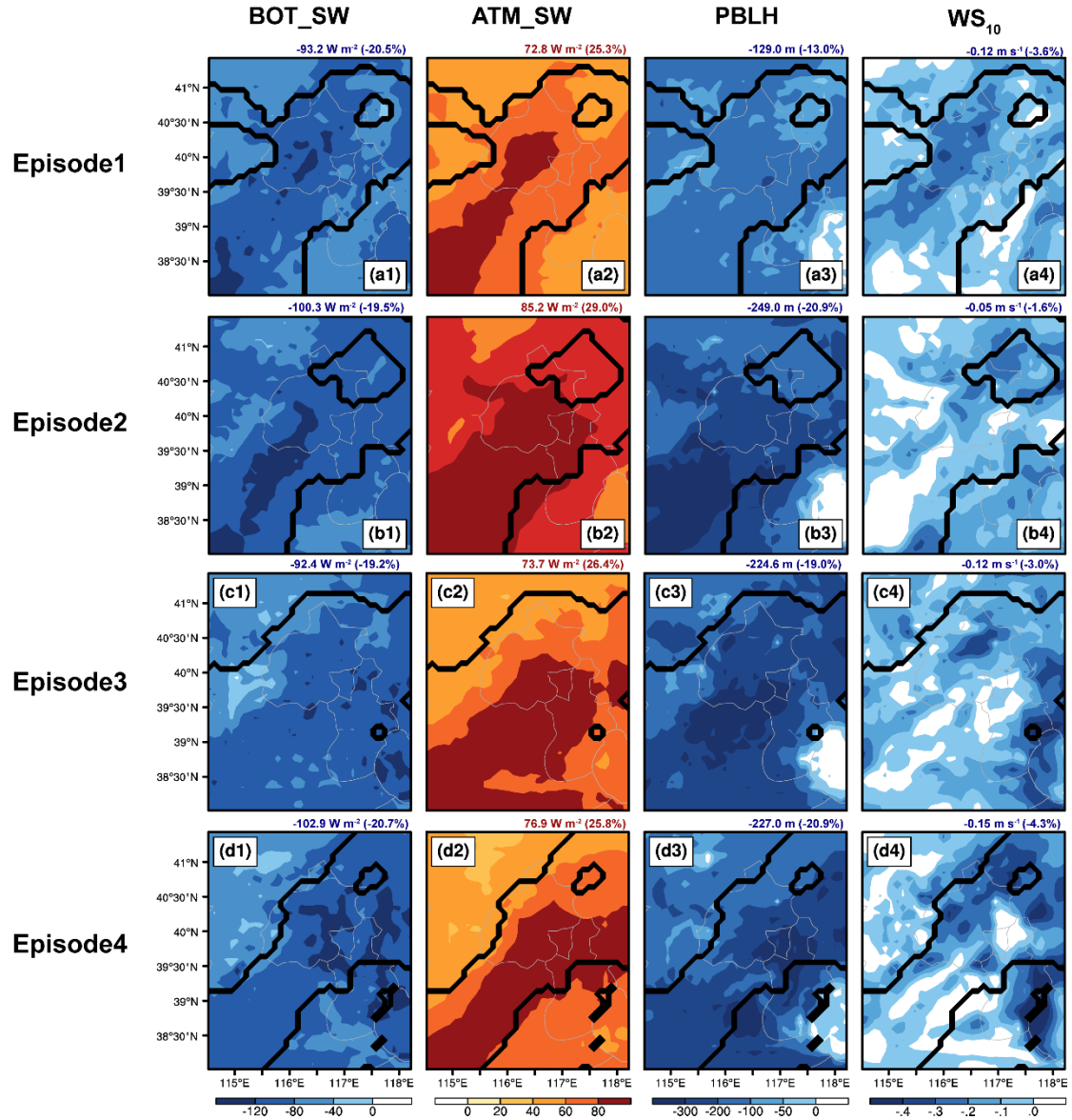
Figure 4. The impacts of aerosol-radiation interactions on shortwave radiation at the surface (BOT_SW), shortwave radiation in the atmosphere (ATM_SW), PBL height (PBLH), and 10-m wind speed (WS_{10}) in the daytime (08:00-17:00 LST) during 28 July to 3 August 2014 (Episode1), 8-13 July 2015 (Episode2), 5-11 June 2016 (Episode3) and 28 June to 3 July 2017 (Episode4). The regions sandwiched between two black lines are defined as the complex air pollution areas (CAPAs) where the mean daily $PM_{2.5}$ and MDA8 O_3 concentrations in BASE case are larger than 75 μg m^{-3} and 80 ppb. The calculated changes (percentage changes) averaged over CAPAs are also shown at the top of each panel.
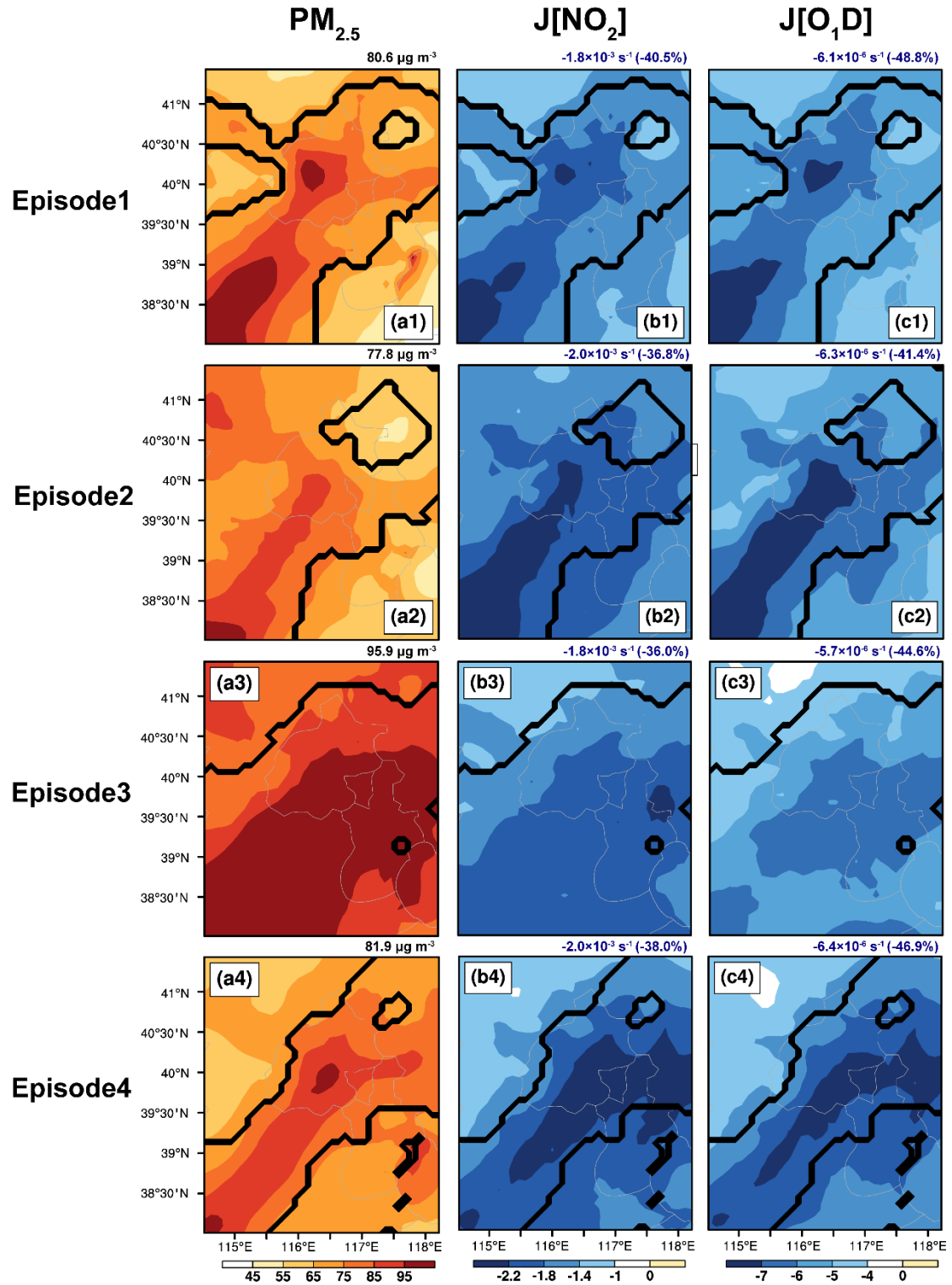
Figure 5. Spatial distributions of (a) simulated surface-layer $PM_{2.5}$ concentrations in BASE cases, and the changes in surface (b) $J[NO_2]$ and (c) $J[O^1D]$ due to aerosol-radiation interactions in the daytime (08:00-17:00 LST) during 28 July to 3 August 2014 (Episode1), 8-13 July 2015 (Episode2), 5-11 June 2016 (Episode3) and 28 June to 3 July 2017 (Episode4). The calculated values (percentage changes) avaraged over CAPAs are also shown at the top of each panel.
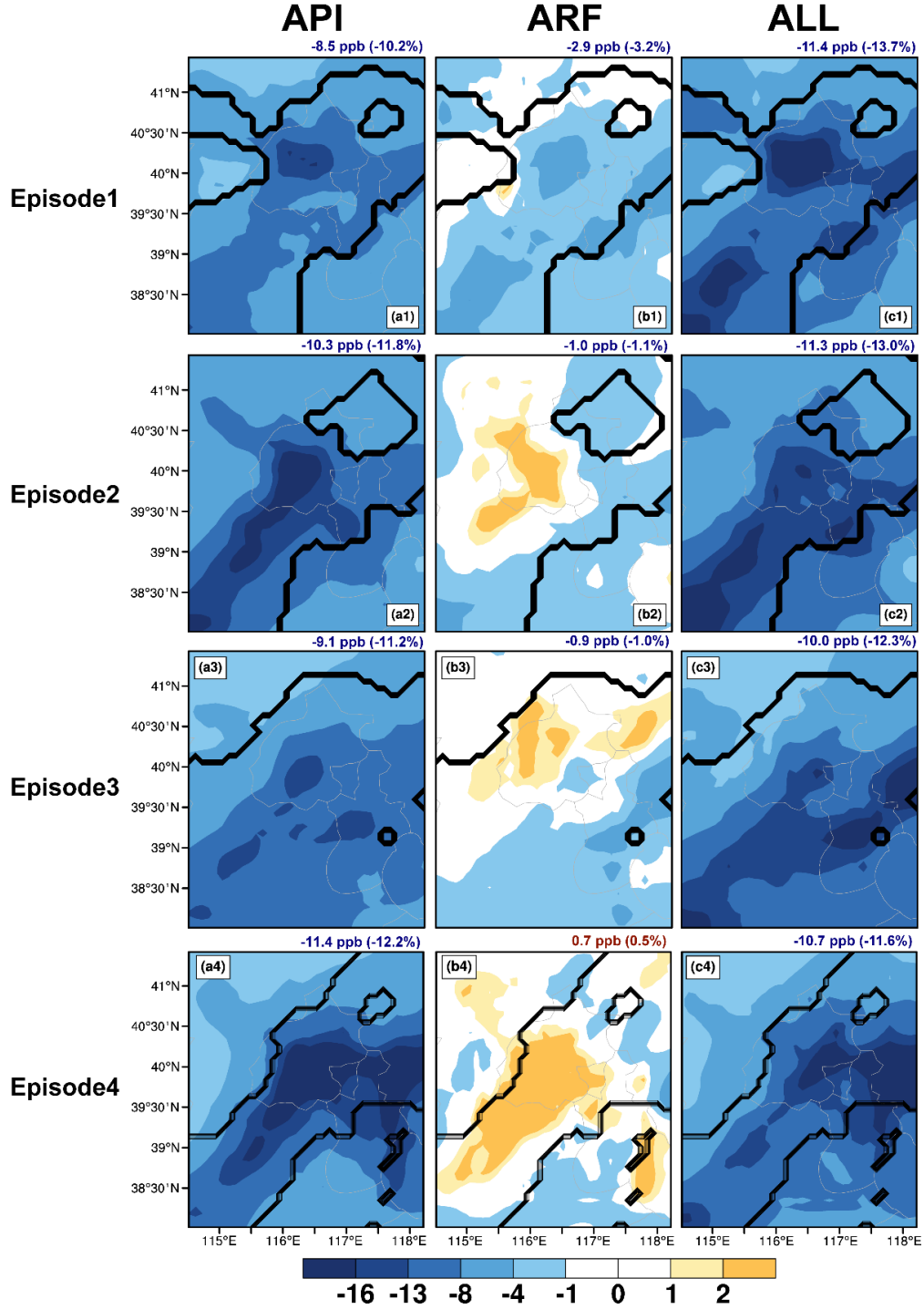
Figure 6. The changes in surface-layer ozone due to (a) aerosol-photolysis interaction (API), (b) aerosol-radiation feedback (ARF), and (c) the combined effects (ALL, defined as API+ARF) in the daytime (08:00-17:00 LST) during 28 July to 3 August 2014 (Episode1), 8-13 July 2015 (Episode2), 5-11 June 2016 (Episode3) and 28 June to 3 July 2017 (Episode4). The changes (percentage changes) in O_3 concentrations caused by API, ARF and ALL avaraged over CAPAs are also shown at the top of each panel.
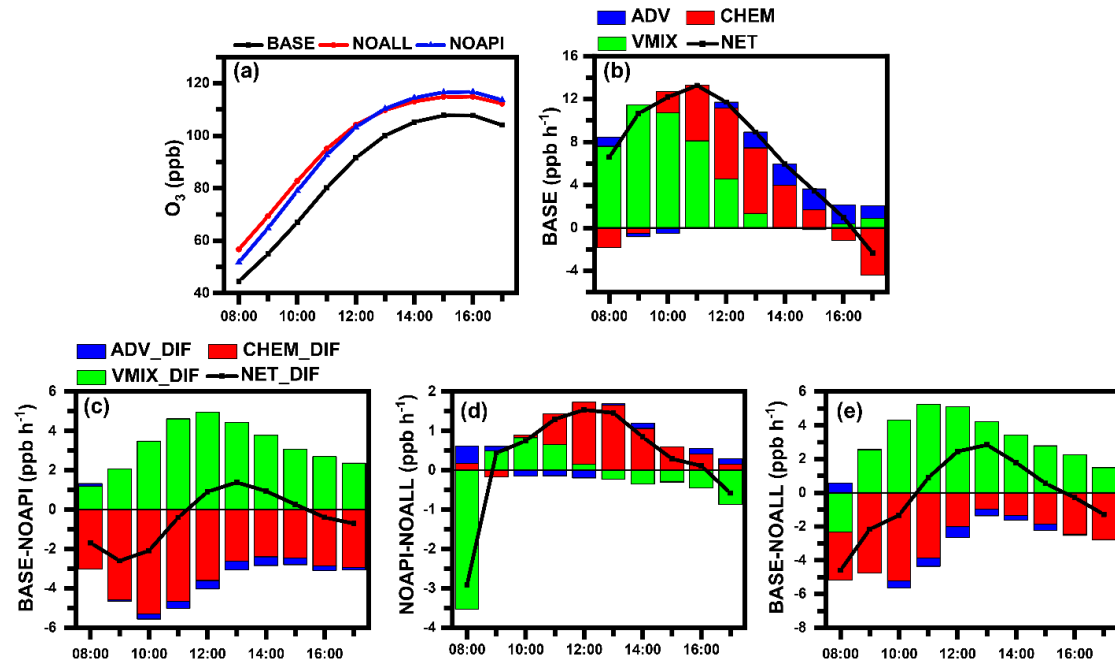
Figure 7. Temporal evolution characteristics of aerosol-radiation interactions on O_3 averaged over the four episodes. (a) Diurnal variations of simulated surface O_3 concentrations in BASE (black dotted line), NOAPI (blue dotted line), and NOALL (red dotted line) cases over CAPAs. (b) The hourly surface O_3 changes induced by each physical/chemical process using the IPR analysis method in BASE case. (c-e) Changes in hourly surface O_3 process contributions caused by API (BASE minus NOAPI), ARF (NOAPI minus NOALL), and ALL (BASE minus NOALL) over CAPAs during the daytime (08:00-17:00 LST). The black lines with squares denote the net contribution of all processes (NET, defined as VMIX+CHEM+ADV). Differences of each process contribution are denoted as VMIX_DIF, CHEM_DIF, ADV_DIF, and NET_DIF.
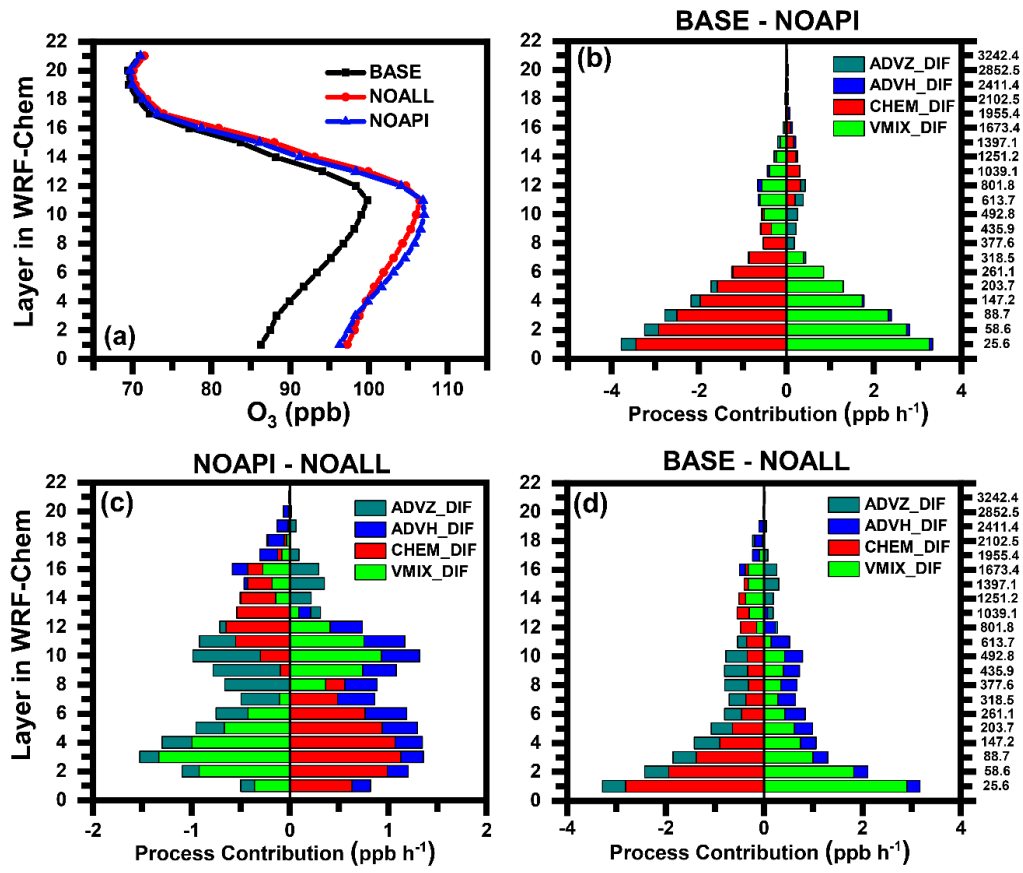
1

Figure 8. The impacts of aerosol-radiation interactions on vertical O_3 averaged over
the four episodes. (a) Vertical profiles of simulated O_3 concentrations in BASE (black
dotted line), NOAPI (blue dotted line), and NOALL (red dotted line) cases over
CAPAs. (b-d) Changes in O_3 budget due to API, ARF, and ALL over CAPAs during
the daytime (08:00-17:00 LST). Differences of each process contribution are denoted
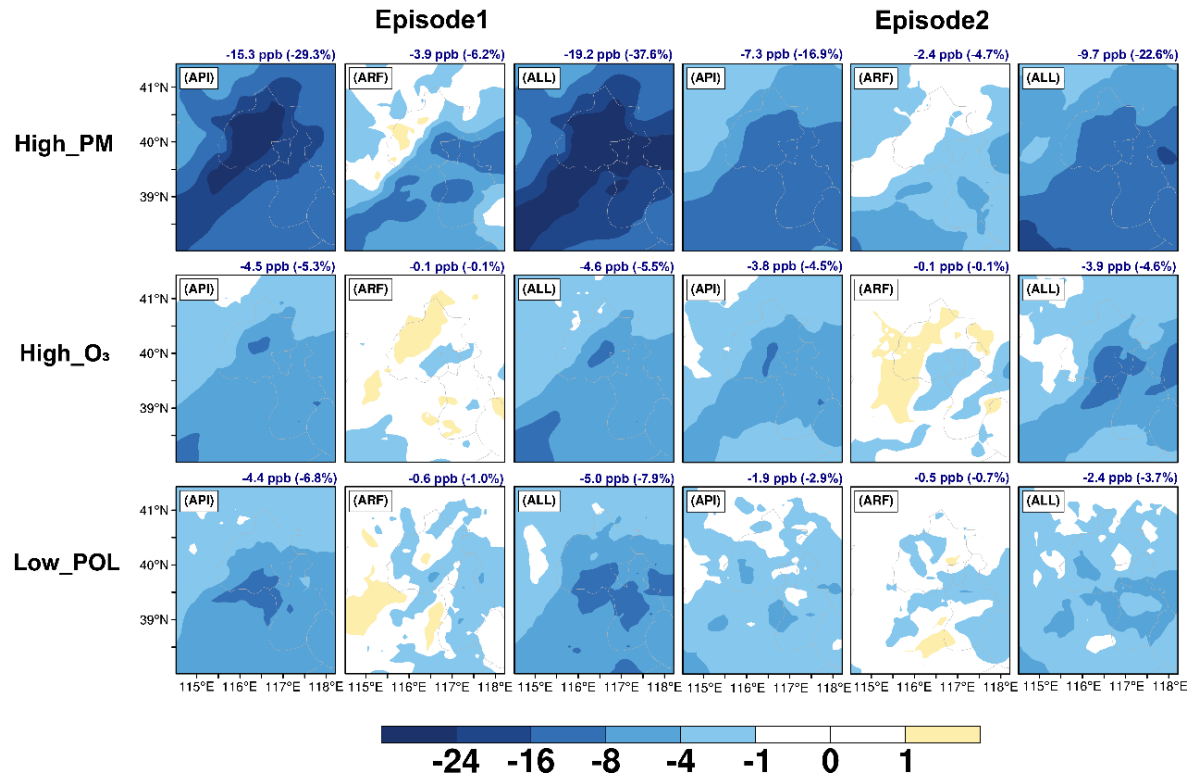by ADVZ_DIF, ADVH_DIF, CHEM_DIF, and VMIX_DIF.

8

Figure 9. The changes in surface-layer O_3 due to aerosol-photolysis interaction (API), aerosol-radiation feedback (ARF), and the combined effects (ALL, API+ARF) in the daytime (08:00-17:00 LST) of 7-12 October 2014 (High_PM_Episode1), 7-11 April 2014 (High_PM_Episode2), 13-18 June 2016 (Low_POL_Episode1), 13-17 July 2016 (Low_POL_Episode2), 15-21 June 2017 (High_O_3_Episode1), and 12-17 July 2017 (High_O_3_Episode2). The changes (percentage changes) in O_3 concentrations caused by API, ARF and ALL avaraged over the entire simulated domain are also shown at the top of each panel.